Phase separation over an extended compositional range: Studies of the $Ca_{1-x}Bi_xMnO_3$ ($x \leqslant 0.25$) phase diagram

P. N. Santhosh, J. Goldberger, and P. M. Woodward
Department of Chemistry, The Ohio State University, 100 West 18th Avenue, Columbus, Ohio 43210-1185

T. Vogt
Department of Physics, Brookhaven National Laboratory, Upton, New York 11973

W. P. Lee and A. J. Epstein
Department of Physics, The Ohio State University, 174 West 18th Avenue, Columbus, Ohio 43210-1185
and Department of Chemistry, The Ohio State University, 100 West 18th Avenue, Columbus, Ohio 43210-1185
(Received 12 April 2000)

Phase transitions on the electron-doped side of the $Ca_{1-x}Bi_xMnO_3$ system ($x \leqslant 0.25$) have been investigated using high-resolution synchrotron x-ray and neutron powder-diffraction techniques, electrical transport and magnetic susceptibility measurements. At room temperature all samples investigated were single phase, paramagnetic conductors ($\rho < 0.1\ \Omega$ cm), isostructural with $GdFeO_3$ (space group *Pnma*). The Mn-O-Mn angles remain nearly constant from $x=0$ to $x=0.25$, while the Mn-O distances steadily increase with the Mn^{3+} content. Three distinct phases are observed at 25 K. The first one, observed from $0.15 \geqslant x \geqslant 0.03$, is characterized by the absence of charge and orbital ordering, a canted *G*-type antiferromagnetic spin structure, and delocalized electron transport. The second phase, observed from $0.25 \geqslant x \geqslant 0.12$ (single phase at $x=0.18$), is characterized by pronounced orbital ordering, a *C*-type antiferromagnetic spin structure, and insulating behavior. The third low-temperature phase, observed for $x \geqslant 0.20$, is characterized by orbital and magnetic ordering similar to the Wigner crystal structure previously observed for $Ca_{0.67}La_{0.33}MnO_3$, but with a $4a \times b \times 2c$ unit cell. The most striking feature of the phase diagram is the wide compositional range over which low-temperature phase separation is observed. Only those samples with $x < 0.12$ and $x=0.18$ did not undergo phase separation upon cooling. We show that this behavior cannot be attributed to compositional variations, and therefore, propose that anisotropic strain interactions between crystallites may be partially responsible for this behavior.

I. INTRODUCTION

The discovery of colossal magnetoresistance[1–3] (CMR) in manganese perovskites, $A_{1-x}L_xMnO_3$ (L = trivalent rare-earth cation; A = divalent alkaline-earth cation), has prompted renewed interest in these materials. The intricate relationships between the structural, magnetic, and electrical transport properties as a function of temperature, average *A*-site cation radius $\langle r_A \rangle$ and concentration of Mn^{4+} have been extensively studied since their initial discovery in the early 1950's.[4,5] Most of these studies have concentrated on the hole-rich region of the $A_{1-x}L_xMnO_3$ ($0.5 < x < 0.8$) phase diagram. These systems are characterized by a strong competition between the charge-ordered and the charge-delocalized states. The charge-ordered state is typically antiferromagnetic and insulating, while the charge-delocalized state is ferromagnetic and metallic. The transition from a paramagnetic insulating state to a ferromagnetic metallic (FMM) state, commonly observed in this region, has been explained within the framework of the double-exchange mechanism,[6] associated Jahn-Teller distortions[7] and electron-phonon coupling (polarons).[8] Nonetheless, a complete understanding of the various magnetotransport properties remains elusive.

In the charge delocalized state, the e_g electrons move freely through the crystal and all manganese ions have the same coordination. The antibonding character of the e_g electrons is isotropically dispersed, and all manganese ions are in a mixed-valence state. Below a particular temperature, T_{CO}, the repulsive Coulombic interactions between carriers (e_g electrons) overcome the kinetic energy of the carriers and electron localization results. This leads to an ordering of Mn^{3+} and Mn^{4+} (electron configurations $t_{2g}^3 e_g^1$ and $t_{2g}^3 e_g^0$, respectively), the details of which depend upon the exact ratio of the ions. In the charge-ordered state, the $Mn^{3+}O_6$ octahedra, where the doubly degenerate e_g states are singly occupied, undergo a significant distortion as required by the Jahn-Teller theorem. This distortion generally occurs via an elongation of one axis of the octahedron (elongation of two Mn-O bonds trans to each other), lowering the energy of the occupied $d_{3z^2-r^2}$ orbital. In most instances the orientation of the long Mn^{3+}-O bonds is ordered cooperatively throughout the crystal in order to minimize the lattice strain associated with this bond elongation. This behavior is referred to as a cooperative Jahn-Teller distortion and/or orbital ordering.[9] As pointed out long ago by Goodenough, the competition between Coulombic interactions (electrostatic energy), strain interactions (elastic energy), and spin interactions (magnetic energy) determines the final configuration of the ground state.[10] The fact that each of these interactions is very sensitive to the doping level and bandwidth, which is in turn dependent upon the Mn-O-Mn bond angles, accounts for the complexity of the $A_{1-x}L_xMnO_3$ phase diagram.

A. Phase separation

de Gennes[11] was the first to discuss the limit of strong ferromagnetic (FM) exchange between itinerant electrons and spins. He suggested that the competition between antiferromagnetic (AFM) superexchange and double exchange leads to a canted AFM state. This state is characterized by canted localized spins forming two sublattices. In other words, the canted AFM state bridges the AFM state ($\theta = 180°$) and the FM state ($\theta = 0°$). The canting angle becomes smaller than 180° as more charge carriers are introduced into the system, explaining the increase of the magnetization as the doping level is increased, in systems such as $La_{1-x}Ca_xMnO_3$. deGennes' model of a canted ground state was criticized by Nagaev[12] and recently by Kagan[13] on the basis of quantum corrections stabilizing the AFM state and allowing for canting only above a critical concentration of charge carriers. Recently a picture is emerging that a homogeneous canted AFM state is almost always unstable and tends to phase separate into a mixture of antiferromagnetic and ferromagnetic/canted states. As a consequence, the charge transport and metal-insulator transition would be better described in terms of percolation and not as the property of a pure state.[13,14] Phase separation has been suggested to occur in the cuprates,[15] nickelates[16] as well as the manganates, and is on the rise as a paradigm for the ground state in strongly correlated electron systems. In the $La_{1-x}Ca_xMnO_3$ system phase separation has been observed using small-angle neutron scattering[17] and scanning tunneling spectroscopy.[18]

B. Previous studies of electron-doped manganites

Recently the electron-doped region of the manganate phase diagram ($0 > x > 0.3$) has attracted a great deal of interest. This has been fueled by the discovery that CMR could occur in electron-doped as well as hole-doped samples.[19] Nonetheless, there are several unresolved issues associated with the phase transitions and charge ordering behavior in this region of the phase diagram. The observation of charge, orbital, and magnetic ordering in electron-doped manganates dates back to the seminal work by Wollan and Koehler[20] on the $La_xCa_{1-x}MnO_3$ system. The end member, $CaMnO_3$, adopts the *G*-type antiferromagnetic structure ($T_N \sim 110$ K), where each manganese ion is coupled antiferromagnetically to its six near-neighbor manganese ions.[43] Over the compositional range $0.5 \geqslant x \geqslant 0.22$ a charge-ordered (CE)-type antiferromagnetic structure was observed. This magnetic structure is associated with the charge-ordered arrangement of Mn^{3+}/Mn^{4+} seen predominantly at $x = 0.5$. At $x = 0.20$ a *C*-type antiferromagnetic structure prevails. Finally, when $x < 0.1$ the *G*-type structure of $CaMnO_3$ is observed. Figure 1 provides a schematic illustration of the competing magnetic structures in the $La_xCa_{1-x}MnO_3$ system. Goodenough predicted that the CE-type phase would be stable over the compositional range $0.5 \geqslant x > 0.25$, the *C*-type phase from $0.25 \geqslant x > 0.1$, and the *G*-type for $x < 0.1$. Furthermore, he went on to state that phase separation should be observed over a very small region near $x = 0.25$ (CE-type and *C*-type) and in the range $0.15 < x < 0.1$ (*C*-type and *G*-type).[10]

Maignan and co-workers have studied the magnetic and electrical properties of a number of other electron-doped systems (rare earth's from Eu to La).[22] They find a ferromagnetic metallic (FMM) state in a very small region around $x \sim 0.12$, but the saturation magnetization of these compounds are reminiscent of a canted-antiferromagnet or possibly a phase separation into an antiferromagnetic phase and a ferromagnetic phase. A more detailed magnetic study on the $Sm_xCa_{1-x}MnO_3$ system, in the region $0 < x < 0.1$, points toward a cluster glass metallic state, and a lack of long-range ferromagnetic order.[23] Phase separation is a distinct possibility, considering the fact that this regime of electron-doping falls in the region which has been predicted to exhibit phase separation behavior.[14] Finally, they have shown that upon cooling $Sm_{0.15}Ca_{0.85}MnO_3$ transforms to an orbitally ordered, *C*-type AFM state, but no evidence of long-range charge ordering was observed.[44]

Following the discovery of stripelike features observed in TEM pictures of $La_{0.33}Ca_{0.67}MnO_3$ and $La_{0.25}Ca_{0.75}MnO_3$,[24]

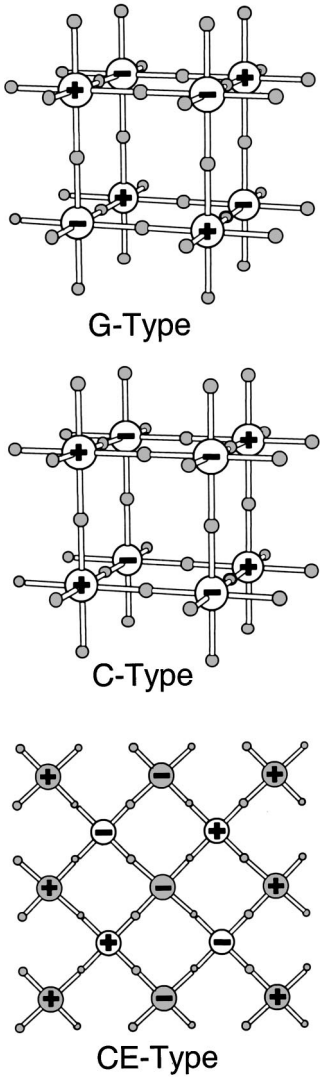

FIG. 1. Schematic diagrams of the *G*, *C*, and CE-type antiferromagnetic structures. For the latter structure only the ions in the *ac* plane are shown, layers above and below the plane are coupled antiferromagnetically. The large spheres represent the transition metal ion, the small shaded spheres oxygen, and the *A*-site cations have been omitted for clarity. For the CE-type structure the Mn^{3+} and Mn^{4+} ions are shown as shaded and white spheres, respectively.

the $La_xCa_{1-x}MnO_3$ system evolved as a model system to understand the various interactions occurring in the electron-doped manganates. The stripelike features were initially explained with a bistripe model where Mn^{3+}-rich regions are separated by Mn^{4+} regions in order to minimize lattice strain. This model allows the structure to respond to changes in the Mn^{3+}/Mn^{4+} ratio by varying the width of the Mn^{4+} regions.[24] Low-temperature neutron-diffraction experiments have confirmed the antiferromagnetic nature of the electron-doped manganate, $La_{0.33}Ca_{0.67}MnO_3$. In the antiferromagnetic structure, the *a* lattice parameter is tripled and the *c* parameter is doubled, with respect to the average crystallographic unit cell. Below the charge-ordering temperature, T_{CO}, the occupied d_{3x2-r2} and d_{3z2-r2} orbitals order in the *ac* plane, and x-ray-diffraction superlattice peaks indicate a tripling of *a* lattice parameter. These high-resolution synchrotron x-ray and neutron-diffraction results provide strong evidence that the ''bistripe model'' is not a correct description of the crystal structure of $La_{0.33}Ca_{0.67}MnO_3$. Instead a detailed analysis based on combined Rietveld refinements, indicates that a ''Wigner crystal'' model explains the data more accurately.[25] Nonetheless, the origin of the stripelike features in the TEM images is still not clear. It is possible that the bistripe model is observed in certain domains or that one needs to take into account changes introduced by imaging conditions such as crystal thickness, orientation and microscopy aberrations and carefully simulate images based on dynamic diffraction theory.[26]

$Bi_xCa_{1-x}MnO_3$ is an electron-doped manganite resembling $La_xCa_{1-x}MnO_3$, due to the fact that the oxidation state and the ionic radius of bismuth are very similar to lanthanum.[27,28] Though, unlike La^{3+} ions, Bi^{3+} ions have a tendency to adopt asymmetric coordination environments to accommodate the development of a stereoactive electron lone pair. Using elastic and inelastic neutron-scattering techniques, charge-ordering and *C*-type magnetic ordering have been observed in $Bi_xCa_{1-x}MnO_3$ single crystals with $x=0.26$, 0.24, and 0.18.[29] However, structural details of the charge-ordered state were not presented. TEM images of a $Bi_{0.20}Ca_{0.80}MnO_3$ sample indicated a quadrupling of one of the unit-cell dimensions, consistent with the Goodenough[10] and Jirak[21] models for Mn^{3+}/Mn^{4+} charge ordering in the *C*-type phase.[28] Furthermore, they also saw evidence for long-range periodic structures with 32- and 36-fold periodicity, with respect to the original unit cell, implying a very complex charge-ordering arrangement. Phase separation behavior into ferromagnetic and antiferromagnetically ordered domains were observed by optical measurements in $Bi_{0.24}Ca_{0.76}MnO_3$,[30] consistent with theoretical predictions. Most recently, charge-ordering has been seen by x-ray-scattering techniques in $Bi_{0.24}Ca_{0.76}MnO_3$.[31] In this latter study the authors claim that the charge-ordered state corresponds to the bistripe model, although it is not obvious that a Wigner-crystal type charge ordering is inconsistent with their data.

C. Scope of the present work

Despite the fact that electron-doped manganites including the (Bi, Ca)MnO_3 system have been previously studied, there are still many unanswered questions: Does charge ordering occur and if so what are the charge ordered, crystallographic structures that correspond to the *C*-type and CE-type magnetically ordered states? If more than one charge-ordered structure exists, over what compositional range is each structure stable? How wide are the compositional ranges over which phase separation occurs? What are the details of the crystallographic and magnetic structure of the ferromagnetic metallic state that has been suggested to exist near $x=0.10$? This work is an attempt to answer these question in a comprehensive manner. To address these issues we have investigated the phase diagram of $Ca_{1-x}Bi_xMnO_3$ from $x=0$ to $x=0.25$ using variable temperature, high-resolution synchrotron x-ray and neutron powder-diffraction techniques, electrical transport, and magnetic-susceptibility measurements.

II. EXPERIMENTAL

Polycrystalline samples of $Ca_{1-x}Bi_xMnO_3$ with $x=0.03$, 0.06, 0.09, 0.12, 0.15, 0.18, 0.20, 0.22, and 0.25 were synthesized from stoichiometric quantities of $CaCO_3$, MnO, and Bi_2O_3 using a conventional ceramic technique. Bi_2O_3 was added in 20% excess for $0.03 \leqslant x \leqslant 0.12$, and 10% excess for $0.15 \leqslant x \leqslant 0.25$, to compensate for the loss of bismuth oxide, due to sublimation. Initial annealing cycles were carried out in air at 1100 °C. They were followed by consecutive heat treatments for 12 h in the range 1200–1270 °C. During all heat treatments the crucibles were covered with lids and pellets were buried in loose powder to reduce the bismuth loss. Cation stoichiometries were confirmed by inductively coupled plasma analysis. Resistivity measurements were carried out between 300 and 5 K using the standard four-probe method. dc magnetization measurements were performed using a superconducting quantum interference device magnetometer in a field of 100 Oe in the same temperature range.

High-resolution synchrotron x-ray powder-diffraction data were collected at the X7A beamline located at the National Synchrotron Light Source at Brookhaven National Laboratory. Monochromatic radiation was obtained from a channel-cut double crystal Si (111) monochromator, oriented to give a wavelength of 0.79921 Å. The samples were loaded into glass capillaries (diameter$\approx$0.2 mm). Variable temperature measurements were obtained by mounting the capillary into a closed-cycle helium cryostat in transmission geometry. The capillary was rotated continuously in the cryostat by ± 10 degrees to minimize preferred orientation effects.

Neutron powder-diffraction data were collected on samples with $x=0.06$, 0.12, and 0.25, using the high resolution diffractometer BT1, located at the NIST Center for Neutron Research (NCNR), in Gaithersburg, Maryland. The BT1 diffractometer is equipped with a bank of 32 detectors and horizontal collimators, with an in-pile collimation of 14′. The detector bank is stepped in 0.05° increments and the sample is mounted inside a vanadium can. Both the Ge(311) monochromator ($\lambda = 2.077$ Å) and the Cu(311) monochromator ($\lambda = 1.540$ Å) were used during the course of the study. Neutron powder-diffraction data on the $x=0.18$ sample were collected at the ANSTO facility in Lucas Heights, Australia. This high-resolution neutron powder diffractometer[32] has a detector bank with 24 ^{3}He detectors. The Ge(115) monochromator provided a wavelength of

TABLE I. Stoichiometry and synthesis temperature (samples annealed in air).

Composition	Annealing Temp. (°C)	ICP analysis (Rel. Mole Frac.) Bi (%)	Ca (%)	Mn (%)
$Bi_{0.03}Ca_{0.97}MnO_3$	1265	0.036	0.964	0.93
$Bi_{0.06}Ca_{0.94}MnO_3$	1265	0.067	0.933	0.988
$Bi_{0.09}Ca_{0.91}MnO_3$	1260	0.098	0.902	1.034
$Bi_{0.12}Ca_{0.88}MnO_3$	1260	0.140	0.860	1.000
$Bi_{0.15}Ca_{0.85}MnO_3$	1250	0.148	0.852	1.073
$Bi_{0.18}Ca_{0.82}MnO_3$	1230	0.188	0.812	1.021
$Bi_{0.22}Ca_{0.78}MnO_3$	1220	0.240	0.760	1.017
$Bi_{0.25}Ca_{0.75}MnO_3$	1205	0.246	0.754	1.013

1.887 Å. The x-ray and neutron refinements of the crystallographic and magnetic structure were performed using the Rietveld method, as implemented in the GSAS software suite.[33]

III. RESULTS

A. Stoichiometry

Sample stoichiometries and purities were investigated using inductively coupled plasma (ICP) spectrochemistry measurements, synchrotron x-ray and neutron diffraction refinements. The results are given in Table I along with the final sintering temperature of each sample. The synchrotron x-ray-diffraction measurements showed the presence of minute levels of a secondary phase(s) in many of the samples. These impurity diffraction peaks appear to reach a maximum in the $x=0.03$ sample where the intensity of the strongest reflection in the impurity phase is 0.3% of the intensity of the strongest reflection of the majority perovskite phase. It is difficult to unambiguously identify the impurity phase(s) from such weak peaks. However, in many of the samples it appears as though the impurity is $CaMn_2O_4$, or some modification of this phase. From this observation we estimate the impurity levels to be on the order of a few percent at most. The impurity levels are almost undetectable in the $x=0.06$, 0.09, and 0.12 samples.

The ICP results indicate that the cation stoichiometries are quite close to the target values. The ICP analysis was repeated in order to estimate the precision of this technique. The discrepancies between runs 1 and 2 were generally less than or equal to 0.01, which is of a similar order of magnitude as the differences between the ICP stoichiometry and the target stoichiometry. This confirms our assumption that the excess Bi_2O_3 volatilizes during synthesis. The only exceptions are the $x=0.03$ sample which appears to have Mn vacancies and the $x=0.15$ sample which appears to have Bi/Ca vacancies. However, as detailed below we do not feel these deviations correspond to actual stoichiometry deviations in the perovskite phase.

To check for the possibility of oxygen vacancies, the oxygen content was refined in those samples where neutron diffraction data were collected ($x=0.06$, 0.12, 0.18, and 0.25). In each case the oxygen content refined to a value slightly ($\sim$ 1–2%) greater than 1 oxygen per site, and there was very little improvement in the fit to the observed diffraction pattern. This is a strong indication that oxygen vacancies are not present.

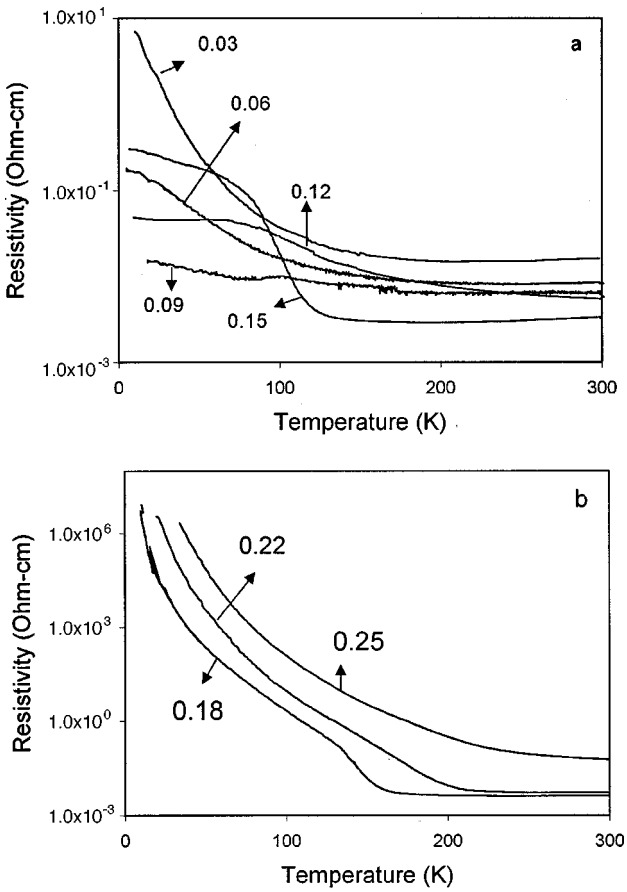

FIG. 2. Resistivity data measured from 300 to 10 K for $Ca_{1-x}Bi_xMnO_3$ samples with (a) $x=0.03$, 0.06, 0.09, 0.12, 0.15, and (b) $x=0.18$, 0.22, and 0.25.

Finally, consider the progression in unit-cell volume of the majority phase, which is very sensitive to the Mn^{4+}/Mn^{3+} ratio. The room-temperature unit-cell volume, discussed in Sec. III D and shown in Fig. 4, shows a linear Vegard's law dependence from $x=0.03$ to $x=0.22$. This is strong evidence for a smooth progression in the Mn^{3+} content. This data when combined with the neutron refinement results, and the general trends of the ICP data, provides compelling evidence that the stoichiometries are quite close to the intended values. It would appear that the discrepancies in the ICP values for $x=0.03$ and $x=0.15$ samples do not reflect real stoichiometric deviations in the perovskite phase. They are likely caused by the presence of minority phase(s) with a different Bi/Ca/Mn ratio.

B. Resistivity

Figures 2(a) and 2(b) show the resistivity of $Bi_xCa_{1-x}MnO_3$ compositions ($x=0.03$ to 0.25) measured from 300 to 5 K. The $Bi_{0.25}Ca_{0.75}MnO_3$ sample does not show a slope change, characteristic of charge-ordering transitions exhibited by many electron-doped systems.[34] Rather, the $d\ln\rho/dT^{-1}$ curve reveals a broad peak at the charge-ordering transition. The $Bi_{0.22}Ca_{0.78}MnO_3$ and

$Bi_{0.18}Ca_{0.82}MnO_3$ samples do show a slope change at the CO transition, with $x=0.18$ exhibiting the sharpest transition. The transition temperatures, T_{CO}, as determined from the resistivity data, for the $x=0.22$ and 0.18 samples are 200 and 145 K, respectively. The increase in resistivity below the charge-ordering transition is ~8 orders of magnitude, which is typical of many type-II charge-ordered systems.[35] In Fig. 2(a), the $x=0.12$ and 0.15 samples show a significantly smaller increase in the resistivity upon cooling below the transition, only about two orders magnitude. A possible explanation for this phenomenon is the coexistence of charge-delocalized and charge-ordered regions. The resistivity of the $x=0.09$ sample is relatively temperature independent, and has the smallest low-temperature resistivity of any sample observed in the study. As the doping level is further decreased the low-temperature resistivity begins to increase. The resistivity curve of the $x=0.03$ sample is similar to the resistivity behavior of $CaMnO_3$.[36] These results are in agreement with earlier studies of electron-doped systems, where delocalized electron transport was observed at low temperature in samples with doping levels near $x=0.10$.[36] The decrease in resistivity for these samples has been attributed to the presence of ferromagnetic metallic domains coexisting with antiferromagnetic insulating domains.[22]

C. Magnetization

The magnetization data of the above samples are given in Fig. 3. The $x=0.25$, 0.22, and 0.18 samples show a decrease in the susceptibility at the charge-ordering transition, which produces a broad maximum in the magnetization data. Such a peak is typically observed in the magnetic susceptibility data of compounds that undergo type-II charge-ordering (e.g., $Nd_{0.5}Ca_{0.5}MnO_3$). It occurs due to the change from short-range ferromagnetic fluctuations above the transition to short-range antiferromagnetic in the charge-ordered state.[29] The magnetic transition temperatures correspond well with those determined from resistivity data (see Table II). For the $x=0.18$ composition there is a visible hump around 150 K corresponding to the antiferromagnetic Neél temperature (T_N). We are not able to clearly distinguish this feature in the other compositions. This could be due to the fact that for higher x compositions, the charge-ordering transitions are broad transitions and the antiferromagnetic peak may be embedded in the broad peak corresponding to charge-ordering transition.

The $x=0.15$ and 0.12 samples show an increase in the spontaneous magnetization as the temperature is lowered, in sharp contrast to the behavior of the more heavily doped samples. This behavior has been reported previously in other electron-doped manganates, and attributed to the presence of a cluster-glass metallic state[23] characterized by the coexistence of isolated ferromagnetic clusters in a largely antiferromagnetic matrix (''spin bags''). Such a state is not unrealistic in light of the fact that we are near the concentration where phase separation is expected. The $x=0.09$, 0.06, and 0.03 samples also show a spontaneous moment at low temperature, but the susceptibility steadily decreases as the value of x decreases from 0.12–0.03. Interestingly, the last three samples also show an order of magnitude decrease in their room-temperature susceptibility.

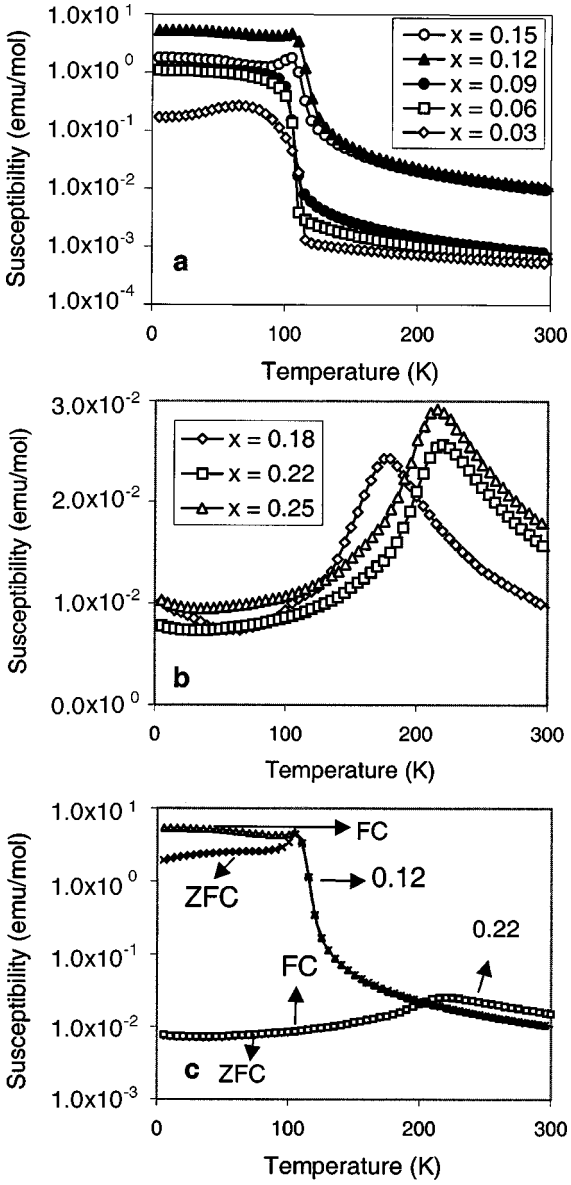

FIG. 3. Magnetic susceptibility (χ) data measured in a field of 100 G for (a) $x=0.03$, 0.06, 0.09, 0.12, and 0.15; (b) $x=0.18$, 0.22, and 0.25; (c) Field-cooled (FC) and zero-field cooled (ZFC) data for $x=0.12$ and 0.22 samples.

The field-cooled (FC) and zero-field cooled (ZFC) data for the 0.25, 0.22, and 0.18 are similar or show only a very small difference, giving evidence for pure antiferromagnetic behavior. The $x=0.15$, 0.12, 0.06, and 0.03 samples show a clear difference between the FC and ZFC curves, characteristic of a cluster glass or a (metallic) canted antiferromagnetic state as observed by Maignan *et al.*[23] The representative examples in each case, $x=0.22$ and 0.12 are shown in Fig. 3(c).

D. Room temperature structural studies

Room-temperature neutron powder diffraction patterns were collected and used in subsequent structural refinements for $Ca_{1-x}Bi_xMnO_3$ samples with $x=0.06$, 0.12, 0.18, and 0.25. Room-temperature synchrotron x-ray-diffraction patterns were collected and analyzed in a similar fashion for the

TABLE II. Transition temperatures from ρ, χ, and x-ray data.

Composition x	Transition temperatures (K)		
	Resistivity	Magnetization	X-ray data
0.03		110[a]	
0.06		110[a]	
0.09		110[a]	110
0.12	130	120[a] (105)	100
0.15	130	120[a] (105)	150
0.18	145	175 (150)	150
0.22	205	220	200
0.25	210	220	220

[a]Spontaneous magnetization observed at these temperatures. The values given in the parenthesis correspond to T_N, antiferromagnetic transition temperature.

samples with $x=0.03$ and 0.06, 0.09, 0.12, 0.18, 0.22, and 0.25. The high-resolution of the x-ray data is ideal for determining accurate lattice parameters as well as assessing the sample homogeneity. Unfortunately, the high degree of pseudocubic symmetry, present in these samples at room temperature, reduces the accuracy of the oxygen positions determined from x-ray data. The neutron data, which are much more sensitive to changes in the oxygen positions, are therefore highly complimentary.

Inspection and analysis of the x-ray-diffraction patterns showed all samples to be single-phase perovskites (neglecting the previously mentioned traces of impurity phases present at roughly the 1% level). The Bragg reflections were sharp and symmetric confirming the excellent compositional homogeneity of the samples. The evolution of the lattice parameters and unit-cell volumes are shown in Fig. 4. The linear increase of the unit-cell volume with increasing x is strong evidence that the Mn^{4+}:Mn^{3+} ratio is continuously evolving as expected from the target compositions. The similarity in the $b/\sqrt{2}$ and c lattice parameters shown in Fig. 4(a) illustrates the high degree of pseudosymmetry present. The system progresses towards a pseudocubic symmetry as x approaches zero. From the profile parameters obtained in the Rietveld refinements we were able to extract $\Delta d/d$ values (equivalent to strain induced by compositional variation) for each sample, using the equations developed in Ref. 37. If we then take $\Delta d/d$ as a measure of the distribution of lattice parameters corresponding to compositional fluctuations in the Mn^{3+}:Mn^{4+} ratio,[38] and determine the relationship between $\Delta d/d$ and x from the lattice parameters shown in Fig. 4(a) we can obtain an upper limit the compositional homogeneity of each sample. The results of this analysis are given in Table III. The long-range compositional fluctuations are on the order of 2%. In other words the composition of an individual crystallite in a sample such as $Bi_{0.12}Ca_{0.88}MnO_3$, might range anywhere from $Bi_{0.1}Ca_{0.89}MnO_3$ to $Bi_{0.13}Ca_{0.87}MnO_3$.

The results of the neutron refinements are contained in Table IV. The continuous increase in the Mn-O bond distances is directly related to the increasing concentration of antibonding e_g electrons. Also note that the three crystallographically distinct distances are very similar, consistent with regular octahedra and the absence of any cooperative

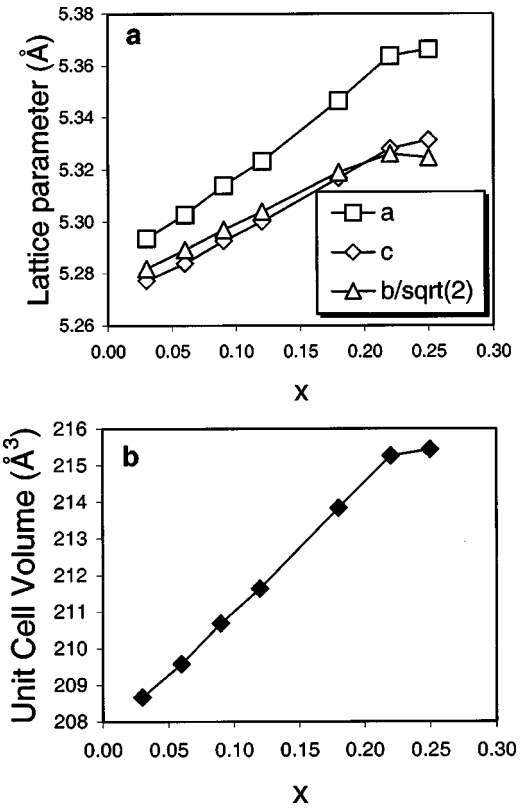

FIG. 4. (a) Unit-cell parameters and (b) unit-cell volume vs x, as determined from room-temperature synchrotron x-ray data.

Jahn-Teller distortion at room temperature. The evolution of the Mn-O-Mn bond angles has important consequences for the physics of this system. Note the extremely small deviation ($\sim 1°$) in bond angle observed over this extended range of composition. Since the Mn-O-Mn bond angles have been shown to be the most influential feature in determining the width of the σ^* band, we are able to change the doping level without significantly changing the bandwidth in this system. Although the reverse situation (changing bandwidth while keeping a constant doping level) is relatively easy to achieve, it is not usually possible in the manganates to tune the carrier concentration independently from the bandwidth. However, as a caveat to this statement it should be noted that despite the unchanging nature of the Mn-O-Mn angles, the band-

TABLE III. Profile parameters (The Gaussian component U and the Lorentzian component X were employed during the refinements. The $\Delta d/d$ values are obtained from the refined values of U, as described in Ref. 37. The X parameter is the d-independent contribution to broadening. It can be related to the crystallite size and the diameter of the capillary.) $\Delta d/d$ values, and the compositional fluctuations for each sample.

x	U	X	$\Delta d/d$	Δx
0.03	50	2.30	0.0008	0.015
0.06	125	3.18	0.0012	0.022
0.09	86	3.09	0.0010	0.018
0.12	101	2.28	0.0011	0.020
0.18	87	2.85	0.0010	0.018
0.22	84	2.97	0.0010	0.018
0.25	162	3.17	0.0014	0.026

TABLE IV. Rietveld refinement results based on room temperature, neutron-diffraction data.

	$x=0.06$	$x=0.12$	$x=0.18$	$x=0.25$
Goodness of fit				
R_{wp}	5.40%	5.16%	6.12%	6.84%
$R(F^2)$	2.20%	2.57%	5.30%	4.52%
Unit-cell dimensions (Å)				
a	5.30035(7)	5.32399(8)	5.3450(1)	5.3652(2)
b	7.4752(1)	7.5006(1)	7.5238(2)	7.5256(3)
c	5.28059(8)	5.29988(8)	5.3166(1)	5.3299(2)
Volume	209.222(5)	211.642(3)	213.80(2)	215.20(3)
Atomic position[a]				
Bi/Ca x	0.0340(2)	0.0335(3)	0.0350(3)	0.0367(4)
Bi/Ca z	0.0068(2)	−0.0055(7)	−0.0073(5)	−0.0054(6)
O_{ax} x	−0.0112(3)	−0.0125(4)	−0.0118(3)	−0.0141(4)
O_{ax} z	0.4346(4)	0.4342(5)	0.4339(4)	0.4308(4)
O_{eq} x	0.7129(2)	0.7137(2)	0.7132(2)	0.7135(3)
O_{eq} y	−0.0344(2)	−0.0343(2)	−0.0352(2)	−0.0350(2)
O_{eq} z	0.2878(2)	0.2859(3)	0.2881(3)	0.2879(3)
Isotropic displacement parameters				
Bi/Ca U_{iso}	0.0100(2)	0.0127(5)	0.0124(3)	0.0113(4)
Mn U_{iso}	0.0032(2)	0.0055(5)	0.0097(5)	0.0071(5)
Anisotropic displacement parameters				
$O_{ax}U_{11}$	0.0097(8)	0.023(2)	0.0132(7)	0.017(1)
$O_{ax}U_{22}$	0.001(1)	0.001(1)	−0.001(1)	0.001(1)
$O_{ax}U_{33}$	0.010(1)	0.010(2)	0.017(1)	0.012(1)
$O_{ax}U_{13}$	−0.0003(8)	0.000(1)	0.0029(8)	0.001(1)
$O_{eq}U_{11}$	0.0070(5)	0.0114(7)	0.0129(5)	0.0134(6)
$O_{eq}U_{22}$	0.0065(5)	0.0064(9)	0.0099(5)	0.0077(7)
$O_{eq}U_{33}$	0.0058(5)	0.0070(8)	0.0110(7)	0.0100(6)
$O_{eq}U_{12}$	−0.0015(4)	0.0007(7)	−0.0032(5)	−0.0004(6)
$O_{eq}U_{13}$	−0.0005(5)	0.0031(6)	0.0002(5)	−0.0009(6)
$O_{eq}U_{23}$	0.0012(5)	−0.0019(8)	0.0024(5)	0.0003(7)
Bond distances (Å)				
Mn-O_{ax}	2×1.9014(4)	2×1.9085(5)	2×1.9146(4)	2×1.9187(5)
Mn-O_{eq}	2×1.910(1)	2×1.912(2)	2×1.921(1)	2×1.926(2)
	2×1.907(1)	2×1.918(2)	2×1.928(1)	2×1.933(2)
Mn-O average	1.906	1.913	1.921	1.926
Bond angles (°)				
Mn-O_{ax}-Mn	158.8(1)	158.6(2)	158.5(1)	157.4(1)
Mn-O_{eq}-Mn	157.02(6)	157.49(9)	156.78(8)	157.0(1)

[a]All compounds crystallize in space group *Pnma*, with Mn on the 4*b* site $(0,0,\frac{1}{2})$, Bi/Ca and O_{ax} on the 4*c* site $(x,\frac{1}{4},z)$, and O_{eq} on the 8*d* site (x,y,z).

width is also dependent upon the Mn-O distances, which are directly dependent upon the doping level. Consequently, it is virtually impossible to change the doping level without some perturbation of the bandwidth.

E. Low-temperature studies of the crystal and magnetic structure

Upon cooling from room temperature to 25 K, relatively strong reflections appear in the neutron-diffraction patterns, indicative of long-range magnetic order (see Fig. 5). To determine the details of each magnetically ordered structure we first indexed these magnetic reflections and then compared our results with the observations of Wollan and Koehler.[20] In this manner we were able to identify the type of magnetic structure (*G*-type, *C*-type, etc.) present in each sample. Once the starting model had been identified the magnitude and direction of the magnetic moment were refined using the Rietveld method. The results are given in Table V, fractional coordinates and displacement parameters are contained in Table VI.

Refinements show that the magnetic structure of $Bi_{0.06}Ca_{0.94}MnO_3$ corresponds to a *G*-type arrangement, isostructural with $CaMnO_3$.[43] The refined fit improves somewhat (R_{wp} decreases from 6.59% to 6.36%) if the moments are allowed to cant, as would be expected from the magnetic susceptibility data. Though the pseudocubic symmetry makes unambiguous identification of the orientation of the

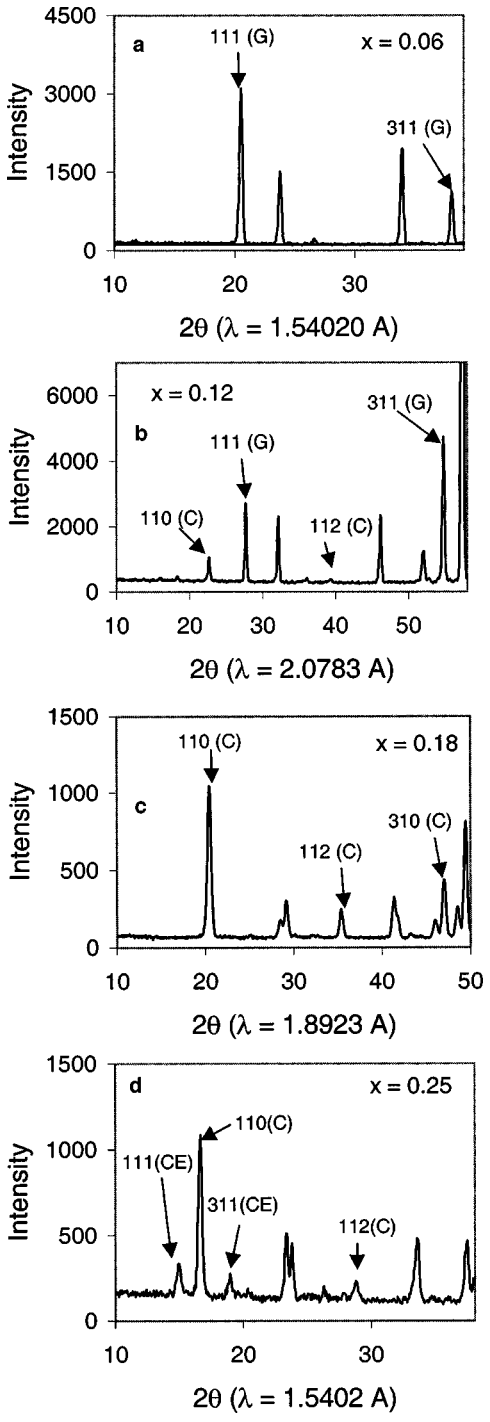

FIG. 5. Low-angle regions of the neutron-diffraction patterns collected at low temperature for samples with doping levels x of (a) 0.06 (10 K), (b) 0.12 (20 K), (c) 0.18 (12 K), and (d) 0.25 (15 K). The angular regions have been chosen to cover approximately the same range of d spacing. Significant magnetic reflections and the phase they are associated with are marked.

moment difficult, the best fit was obtained with the primary component of the moment directed parallel to the c axis. The crystal structure is isostructural with $CaMnO_3$ and shows no evidence for charge and/or orbital ordering.

The $x=0.12$ sample exhibits reflections suggesting the presence of both G-type and C-type structures. Splitting of the nuclear peaks is observed confirming the low-temperature phase separation of this sample. The canted G-type phase (87 wt. %) is the majority phase, while the antiferromagnetic C-type phase (13 wt. %) is the minority phase. The crystal structure of the minority phase adopts a monoclinic, $a \cong \sqrt{2}a_P$, $b \cong 2a_P$, $c \cong \sqrt{2}a_P$, $\beta \cong 91°$, unit cell (space group $P2_1/m$). The monoclinic dimensions of this cell, which are more clearly observed in the high-resolution x-ray data, are a consequence of orbital ordering, as discussed in greater detail below. Both the crystal and the magnetic structure of the C-type phase are isostructural with $Sm_{0.15}Ca_{0.85}MnO_3$.[44]

The magnetic ordering of the $Bi_{0.18}Ca_{0.82}MnO_3$ sample corresponds to a simple C-type AFM structure. Reflections corresponding to the C-type phase are also present in the neutron-diffraction pattern of $Bi_{0.25}Ca_{0.75}MnO_3$, together with several reflections which cannot be indexed using either the monoclinic or the orthorhombic unit cell. The latter set of magnetic reflections can be indexed using an orthorhombic $4\sqrt{2}a_P \times 2a_P \times 2\sqrt{2}a_P$ unit cell. The dimensions of this unit cell are reminiscent of the magnetic structure elucidated by Radaelli *et al.* for $La_{0.33}Ca_{0.67}MnO_3$,[25] which suggests that the magnetic ordering is of the Wigner-Crystal type. The fact that we observe a quadrupling of the unit cell in the x direction, rather than a tripling as seen for $La_{0.33}Ca_{0.67}MnO_3$, is consistent with the Mn^{4+}:Mn^{3+} ratio of 3:1. To further test the validity of the Wigner-Crystal model a refinement was carried out using the magnetic structure shown in Fig. 6. This model gives a good fit to the observed diffraction pattern, provided the monoclinic C-type phase is included as a minority phase (29 wt. %). Unfortunately the two-phase mixture prevents a detailed refinement of either phase.

Figure 7 shows the temperature evolution of the expanded $2a_P \times 2a_P \times 2a_P$ unit-cell parameters for the $x=0.09$, 0.12, 0.18, and 0.22 samples. The expanded unit cell is plotted to emphasize the directionality of the orbital ordering. Figure 7(a) shows the data corresponding to the $x=0.09$ sample. This sample shows typical thermal-expansion behavior, with the exception of a small discontinuity at ~110 K. This temperature corresponds to the temperature at which spontaneous ordering was observed in the magnetization data. Figure 7(c) shows the temperature evolution of the $Bi_{0.18}Ca_{0.82}MnO_3$ unit-cell parameters. A pronounced increase in the a lattice parameter, accompanied by a decrease in b and c, occurs very close to the temperature where a sharp upturn in the electrical resistivity was observed. This demonstrates the presence of orbital ordering in the low-temperature phase, triggered by localization of the e_g electrons. The observed expansion in one direction and contraction in the other two directions implies ordering of the occupied d_{3x2-r2} orbitals along the edges of the pseudocubic unit cell, consistent with the C-type antiferromagnetic model put forward by Goodenough.[10]

The lattice constant evolution of the $Bi_{0.12}Ca_{0.88}MnO_3$ sample is plotted in Fig. 7(b). Unlike the $x=0.09$ and 0.18 samples, here we see clear evidence for a phase separation near 100 K. The unit-cell dimensions of the majority phase are very similar to those observed in Fig. 7(a) for the $Bi_{0.09}Ca_{0.88}MnO_3$ sample, while the cell constants of the minority phase are analogous to the low-temperature structure of $Bi_{0.18}Ca_{0.82}MnO_3$. Taken together with the neutron data this clearly demonstrates the presence of both a canted G-type phase, and an orbitally ordered, AFM C-type phase at

TABLE V. Rietveld refinement results for the low-temperature orthorhombic phase, based on neutron-diffraction data.

Doping level	$x=0.06$	$x=0.12$		$x=0.18$	$x=0.25$	
Temperature (K)	10	20		12	15	
Wavelength	1.540 Å	2.078 Å		1.887 Å	1.540 Å	
R_{wp}	6.36%	5.42%		8.76%	8.40%	
Unit-cell dimensions (Å) and phase fractions						
Phase fraction	100%	87%	13%	100%	80%	20%
Space group	*Pnma*	*Pnma*	$P2_1/m$[b]	$P2_1/m$[b]	*Pnma*[c]	$P2_1/m$[b]
a	5.29469(7)	5.3141(1)	5.3383(5)	5.3618(1)	5.3855(2)	5.3754(6)
b	7.4555(1)	7.4762(1)	7.4436(6)	7.4560(2)	7.4485(3)	7.452(1)
c	5.26655(8)	5.2806(1)	5.3033(5)	5.3276(2)	5.3437(2)	5.3371(7)
β			91.03(1)	91.286(2)		91.62(1)
Volume	207.895(5)	209.80(1)	210.70(3)	212.93(1)	214.36(2)	213.70(4)
Magnetic structure						
Shubnikov space group[a]	*Pn′ma′*	*Pn′ma′*	$P2_1/m$[b]	$P2_1/m$[b]	*Pm*	$P2_1/m$[b]
M_x (μ_B)	0[e]	0[e]	2.52(5)	2.73(2)	1.94(5)[d]	3.63(8)
M_y (μ_B)	0.76(4)	0.92(5)	0	0	0	0
M_z (μ_B)	2.16(2)	2.08(2)	0	0	0	0
M_{tot} (μ_B)	2.29(2)	2.27(3)	2.52(5)	2.73(2)	1.97(5)	3.54(8)

[a]Shubnikov symmetry is described in Ref. 42. In GSAS the primed symmetry elements are described as red, and the unprimed symmetry elements as black.

[b]Refined lattice parameters for the nuclear structure. The magnetic cell has approximate dimensions $2a_p \times 2a_p \times 2a_p$ and refined to the following values: $x=0.12 \rightarrow a=7.5930(4)$ Å, $b=7.4436(2)$ Å, $c=7.4566(4)$ Å, and $\beta=90.46(6)°$, $x=0.18 \rightarrow a=7.651(2)$ Å, $b=7.453(2)$ Å, $c=7.472(2)$ Å, and $\beta=90.32(3)°$, $x=0.25 \rightarrow a=7.668(8)$ Å, $b=7.451(3)$ Å, $c=7.535(4)$ Å, and $\beta=90.32(6)°$.

[c]Refined lattice parameters from the *Pnma* subcell. The magnetic peaks of the Wigner crystal phase were refined with $4a \times b \times 2c$ cell.

[d]The magnetic moments were constrained to be parallel to *a* and the Mn^{3+} moments were constrained to be equal to the Mn^{4+} moments. Very little improvement in the fit was observed when these constraints were removed.

[e]Due to the pseudocubic symmetry we cannot rule out the possibility that the moment cants in the *x* direction rather than the *y* direction.

low temperature. The $Bi_{0.22}Ca_{0.78}MnO_3$ and $Bi_{0.25}Ca_{0.75}MnO_3$ samples show similar trends in their lattice constant evolution, hence only the $x=0.22$ data are shown in Fig. 7(d). At 200 K the monoclinic phase discussed above emerges as a minority phase, while the majority phase undergoes a sudden decrease in the *b* parameter and a corresponding increase in the *a* and *c* lattice parameters. This is the classic signature of a cooperative Jahn-Teller effect and clearly indicates ordering of the occupied d_{3x2-r2} and d_{3z2-r2} orbitals in the *ac* plane. The temperature where this discontinuity occurs is comparable to the transition temperature observed from the magnetization and resistivity data (see Table II). Figure 8 shows the region of the x-ray diffraction patterns containing the $\overline{2}02/202/040$ reflections. The peak splitting, observed in this figure, confirms the phase separation and the contrasting types of orbital ordering described above.

The expanded unit-cell parameters for the monoclinic phase at 25 K are plotted as a function of *x* in Fig. 9(a). The *b* and *c* parameters remain relatively constant, but the *a* parameter increases with *x* (particularly from 0.15 to 0.22). Such behavior would be expected as the Mn^{3+} concentration increases if all of the occupied e_g orbitals are oriented in the *a* direction. Figure 9(b) shows the variation with *x* in the lattice parameters of the orthorhombic phase at 25 K. Initially ($x \leqslant 0.15$) the unit-cell parameters increase uniformly with *x*. The uniform increase in all three directions with increasing *x* is expected as the concentration of Mn^{3+} increases in the absence of orbital ordering. The pseudo-orthorhombic phase observed for $x \geqslant 0.20$ shows a sharp decrease in the *b* parameter and an increase in both the *a* and *c* parameters, with respect to the *G*-type orthorhombic phase ($x \leqslant 0.15$). This is consistent with a Wigner-crystal-type ordering of the e_g orbitals in the *ac* plane. The unit-cell volume of each phase is plotted as a function of *x* in Fig. 9(c). In addition to the expected increase in unit-cell volume with increasing Mn^{3+} content, we also see that the *C*-type phase consistently has a larger volume than the *G*-type phase and a smaller volume than the CE-type phase, for the same value of *x*. The change in phase fraction of the monoclinic phase with varying *x* is given in Fig. 9(d). This figure shows that the stability of the monoclinic *C*-type phase decreases as the doping level moves away from $x=0.18$ in either direction.

The results discussed above describe in detail the various types of orbital and magnetic ordering observed in the $Bi_xCa_{1-x}MnO_3$ system, but the question of charge ordering

TABLE VI. Fractional coordinates and displacement parameters for the low-temperature majority phase in $x=0.06$, 0.12, and 0.18, as refined from neutron diffraction data. Unit-cell parameters and space groups are given in Table V.

Atom	Site	x	y	z	Occ.	U_{iso}
			$x=0.06$			
			Fractional coordinates and isotropic displacement parameters			
Bi/Ca	$4c$	0.0364(3)	$\frac{1}{4}$	−0.0072(5)	0.06/0.94	0.0043(6)
Mn	$4b$	0	0	$\frac{1}{2}$	1.0	−0.0021(4)
O_{ax}	$4c$	−0.0122(3)	$\frac{1}{4}$	0.4353(4)	1.0	
O_{eq}	$8d$	0.7122(2)	−0.0344(2)	0.2897(3)	1.0	
			Anisotropic displacement parameters			
	U_{11}	U_{22}	U_{33}	U_{12}	U_{13}	U_{23}
O_{ax}	0.0080(7)	0.000(1)	0.001(1)	0	0.000(7)	0
O_{eq}	0.0034(5)	0.0039(6)	0.0029(5)	0.0024(5)	0.0022(5)	−0.0004(5)
			$x=0.12$			
			Fractional coordinates and isotropic displacement parameters			
Bi/Ca	$4c$	0.0370(4)	$\frac{1}{4}$	−0.0069(6)	0.12/0.88	0.0072(5)
Mn	$4b$	0	0	$\frac{1}{2}$	1.0	0.0060(5)
O_{ax}	$4c$	−0.0126(4)	$\frac{1}{4}$	0.4335(5)	1.0	
O_{eq}	$8d$	0.7138(2)	−0.0350(2)	0.2888(3)	1.0	
			Anisotropic Displacement Parameters			
O_{ax}	0.017(2)	−0.001(1)	0.001(1)	0	0.000(1)	0
O_{eq}	0.0054(7)	0.007(1)	0.0096(9)	0.0000(8)	−0.0012(8)	−0.0024(9)
			$x=0.18$			
			Fractional coordinates and isotropic displacement parameters			
Bi/Ca(1)		0.0325(0)	$\frac{1}{4}$	−0.0033(9)	0.18/0.82	
Bi/Ca(2)		0.5361(8)	$\frac{1}{4}$	0.5074(9)	0.18/0.82	
Mn(1)		$\frac{1}{2}$	0	0	1.0	0.0095(7)[b]
Mn(2)		0	0	$\frac{1}{2}$	1.0	0.0095(7)[b]
O(1)		0.4903(7)	$\frac{1}{4}$	0.0678(7)	1.0	0.0048(4)[b]
O(2)		0.9839(6)	$\frac{1}{4}$	0.4277(7)	1.0	0.0048(4)[b]
O(3)		0.2872(4)	0.0396(4)	0.7158(4)	1.0	0.0048(4)[b]
O(4)		0.7872(4)	0.0344(4)	0.7854(5)	1.0	0.0048(4)[b]
			Anisotropic displacement parameters			
Bi/Ca[a]	0.024(2)	−0.004(2)	0.012(2)	0	−0.008(1)	0

[a]The anisotropic thermal parameters for both Bi/Ca sites were constrained to be the same.

[b]The isotropic thermal parameters for Mn(1) and Mn(2) were constrained to be equal, as were the isotropic thermal parameters for the oxygen ions.

has not yet been addressed. The electrical resistance of the $Bi_{0.18}Ca_{0.82}MnO_8$ sample undergoes a sharp increase near 175 K, signaling a first-order electron localization. This is accompanied by orbital ordering, which causes an orthorhombic to monoclinic distortion of the unit cell. We do not observe superstructure reflections in either the x-ray or the neutron-diffraction pattern to confirm the presence of long-range, coherent Mn^{3+}:Mn^{4+} charge ordering. Our results, combined with electron diffraction[21,44] and neutron scattering measurements,[29] suggest that charge ordering does occur locally, but the coherence length of the ordered domains is too small to be detected by diffraction techniques. In a similar vein we do not observe superstructure reflections in the x-ray diffraction patterns of the $x=0.22$ and 0.25 samples.

IV. DISCUSSION

The $Bi_xCa_{1-x}MnO_3$ phase diagram is shown in Fig. 10. Pure $CaMnO_3$ is an antiferromagnetic insulator, which adopts a *G*-type antiferromagnetic structure. Substituting bismuth for calcium introduces carriers into the σ^* conduction band and leads to a corresponding decrease in the resistivity as the carrier concentration increases. The low-temperature resistivity reaches a minimum near $x=0.09$, where it is nearly temperature independent. At the same time the low-temperature spontaneous magnetization steadily increases with increasing x, reaching a value maximum at $x=0.12$. These features are qualitatively consistent with results reported for this and other electron doped manganites. This behavior has been interpreted by some to be indicative of the presence of a ferromagnetic metallic state,[36] as observed in the hole-doped manganates. However, previous investigations have shown that there are some peculiarities associated with the ferromagnetic behavior of samples in this region of the phase diagram, such as the unusually small value of the spontaneous magnetization[23,27,36] and unexplained peaks below T_C in the imaginary part of the susceptibility.[23]

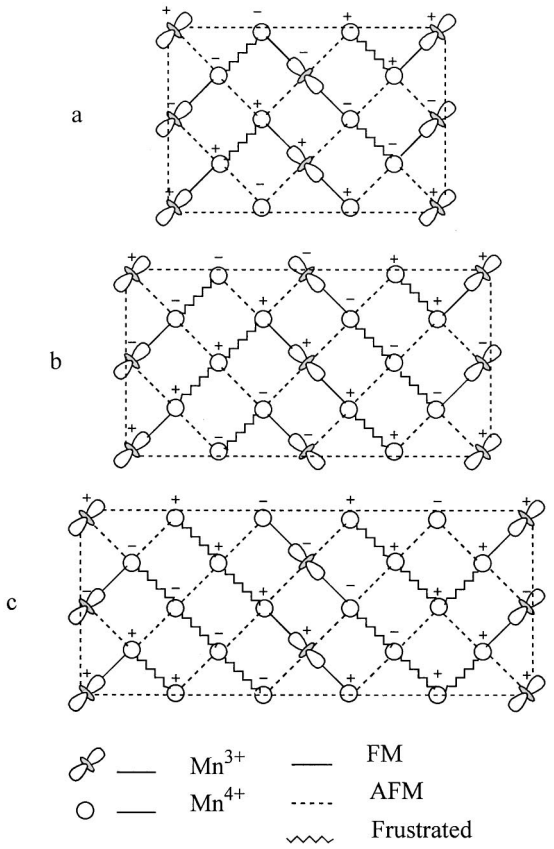

FIG. 6. Models of Wigner crystal charge, orbital and magnetic ordering for $Ca_{1-x}L_xMnO_3$ (L = trivalent ion) samples with a Mn^{3+}:Mn^{4+} ratio of (a) 2:1 ($x=0.33$), (b) 3:1 ($x=0.25$), and (c) 4:1 ($x=0.20$). The percentage of frustrated Mn-O-Mn superexchange interactions in the *ac* plane increases from 16% to 25% to 30% as the doping level decreases.

Neutron diffraction clearly shows that the magnetic ground state is not a simple ferromagnet. Rather the dominant magnetic reflections in the $Bi_{0.06}Ca_{0.94}MnO_3$ diffraction pattern are characteristic of a *G*-type antiferromagnetic structure. Rietveld refinements using a *G*-type structure fit the experimental data quite well, but the fit improves further if a ferromagnetic canting of the moment is allowed. The presence of a canted magnetic structure is consistent with the development of a spontaneous moment in the susceptibility data. The increase in the low-temperature susceptibility with increasing x implies that the degree of canting increases as the doping level increases. Such a model would also qualitatively explain the conducting nature of these samples at low temperature, since in the double-exchange model the transfer integral for a carrier to move from one manganese ion to a neighboring manganese ion is proportional to $\cos(\theta_{ij}/2)$, where θ_{ij} is the angle between spins on the two ions.[39] The combined experimental evidence suggests an increase in canting angle as the doping level increases, leading to an increase of the spontaneous magnetization and the carrier mobility. This behavior is consistent with de Gennes's theoretical predictions for the magnetic ground state of a system with competing antiferromagnetic superexchange and double exchange.[39]

An alternative interpretation of the data in this region of the phase diagram would be to attribute this behavior to a magnetically inhomogeneous system with ferromagnetic domains imbedded in an antiferromagnetic matrix (spin bags). Delocalized electronic conductivity can be realized in such a system in two ways. Either the ferromagnetic metallic domains are mobile (magnetic polarons), or the concentration of such domains could exceed the percolation threshold. In light of the low doping levels required to achieve semimetallic behavior, the former explanation seems more plausible. Using this alternative model one would attribute the observed trends to an increase in the size and/or concentration of the ferromagnetic domains as the doping level is increased. However, it is not clear from our data if the system is better described with a homogeneous canted AFM model or a magnetically inhomogeneous ''spin-bag'' ground state. It should be noted that no evidence of phase separation into FM and AFM domains (unusual peak splitting, asymmetry or broadening) was evident in either the x-ray or the neutron-diffraction data. However, due to the absence of orbital ordering it is not clear if such a subtle phase separation could be readily seen using diffraction methods. Furthermore, theoretical results by Arovas and Guinea indicate that the canted phase may actually be composed of intertwined, nanoscale ferromagnetic and antiferromagnetic domains with different electron concentrations/densities.[40] So that the distinction between the two descriptions may be on a length scale not accessible to diffraction experiments. In the following discussion, we will assume the canted AFM *G*-type model to be the correct one, due to the fact that it is somewhat simpler. *It should be understood, though, that our data do not rule out the alternative description.*

As the doping level increases beyond $x=0.09$ the canted AFM *G*-type state becomes unstable with respect to phase separation. Over the region $0.10<x<0.18$, below the magnetic ordering temperature, a *C*-type antiferromagnetic phase is observed to coexist with the canted *G*-type phase. The temperature dependence of both the resistivity and the susceptibility can be understood more easily in light of the fact that the sample contains both antiferromagnetic insulating regions (*C*-type) and canted metallic regions (*G*-type). Furthermore, the decrease in spontaneous magnetization and low-temperature conductivity with increasing x, are consequences of an increase in the concentration of the AFM *C*-type state, and do not reflect trends in the canted metallic state. It has been suggested by Martin *et al.* that a field-induced transition from a *C*-type to a *G*-type state is responsible for magnetoresistance in the electron-doped manganites.[44] Therefore, we would expect this region of the phase diagram to exhibit magnetoresistive behavior. Indeed Chiba *et al.* observe significant magnetoresistance in a sample of $Bi_{0.125}Ca_{0.875}MnO_3$ below 150 K.[27]

It is not surprising that as the Mn^{3+} content increases and the charge carriers localize, that the AFM *C*-type structure becomes more stable than the *G*-type structure. Every Mn^{3+} ion introduces 2–4 frustrated superexchange interactions into the *G*-type structure. Furthermore, the lattice strain, which originates in the local Jahn-Teller distortion of the Mn^{3+} octahedra, drives the system towards an orbitally ordered state. What is remarkable is the wide compositional range over which the phase separation occurs. It has been clearly demonstrated that this behavior cannot be attributed to subtle compositional fluctuations. The widths of the diffraction

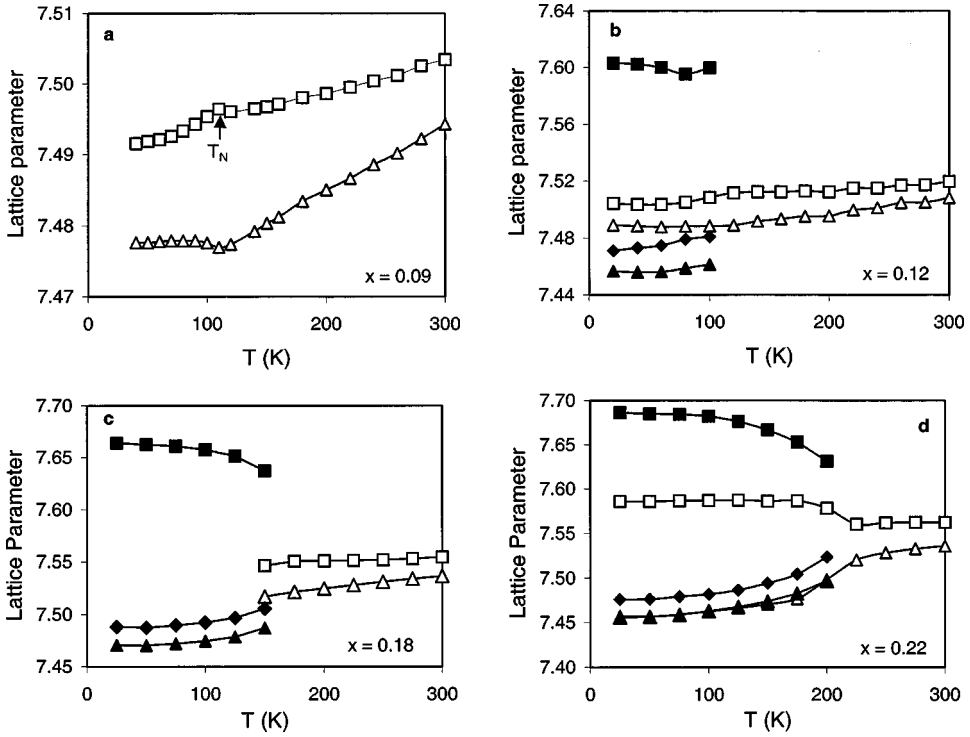

FIG. 7. Lattice constant evolution vs temperature for $Ca_{1-x}Bi_xMnO_3$ samples with (a) $x=0.09$, (b) $x=0.12$, (c) $x=0.18$, and (d) $x=0.22$. The monoclinic (*C*-type) phase is represented by filled symbols, while the orthorhombic (*G*-type) and pseudo-orthorhombic (Wigner crystal type) phases are represented by open symbols. The unit-cell parameters have been transformed to an expanded $2a_P\times 2a_P\times 2a_P$ unit cell for reasons explained in the text. The conversion matrix from the crystallographic unit cell to the expanded cell is $(1\ 0\ 1|0\ 1\ 0|-1\ 0\ 1)$. Note that when the orthorhombic *Pnma* unit cell is transformed in this way the new cell is monoclinic with *a* and *c* parameters which are exactly equal in magnitude ($a=c\neq b$, $\beta\neq 90°$). The *a* parameters are represented by squares, the *b* parameters by triangles, and the *c* parameters by diamonds. For clarity the *c* parameters are not shown when they are equivalent to *a*.

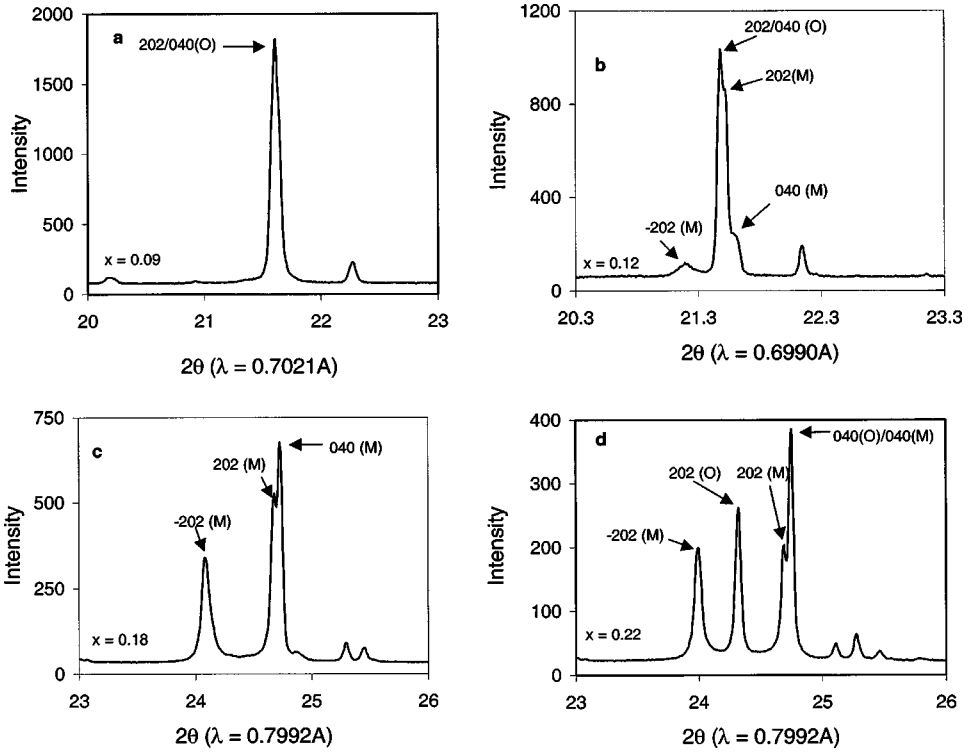

FIG. 8. The orthorhombic (*Pnma*) 202/040 and monoclinic ($P2_1m$) $\bar{2}02/202/040$ reflections from the synchrotron x-ray-diffraction patterns at low temperature for $Ca_{1-x}Bi_xMnO_3$ samples with (a) $x=0.09$, (b) $x=0.12$, (c) $x=0.18$, and (d) $x=0.22$.

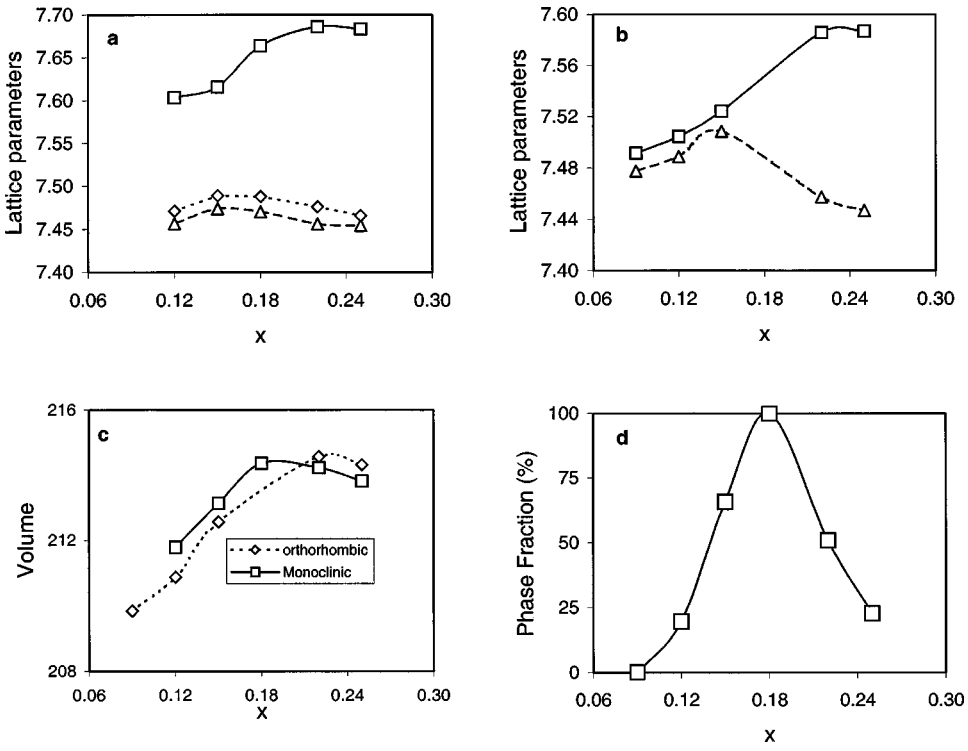

FIG. 9. Low temperature (10–20 K) expanded unit-cell constants of the (a) monoclinic and (b) orthorhombic phases vs x. The a parameters are represented by squares, the b parameters by triangles, and the c parameters by diamonds. See the caption to Fig. 7 for a description of the relationship between the expanded and crystallographic unit cells. The lower two figures show the (c) unit-cell volume and (d) phase fraction of the monoclinic (C-type) phase vs x at low temperature.

peaks indicate relatively large domains for each phase. What then is the driving force behind this phase separation? One possibility is the influence of macroscopic strains on individual crystallites. Due to the fact that the C-type phase exhibits pronounced orbital ordering (a large expansion in the a direction accompanies the charge ordering), whereas the G-type phase does not, the low-temperature macroscopic dimensions of a crystallite will be highly dependent upon its choice of ground state. If the crystallite were to be subjected to a compressive strain parallel to a it should destabilize the C-type phase with respect to the G-type phase, whereas a tensile strain would have the opposite effect. Anisotropic pressure experiments on a single-domain crystal would be the ideal test for probing the validity of this hypothesis, but obtaining a single-domain crystal is a formidable challenge to such an experiment. Thin film studies might be a more reasonable avenue to investigate this possibility.

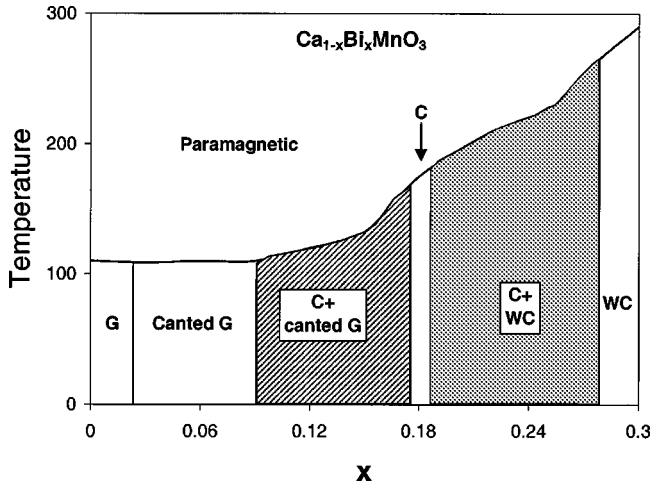

FIG. 10. Proposed phase diagram for the $Ca_{1-x}Bi_xMnO_3$ system.

The $x=0.25$ sample exhibited a Wigner crystal type of ordering with a $4a\times b\times 2c$ unit cell. Figure 6 shows that as you change from $x=0.33$ and a $3a\times b\times 2c$ unit cell to $x=0.25$ and a $4a\times b\times 2c$ cell, the number of frustrated interactions (in the ac plane) increases from 16 to 25%. This increase in frustrated magnetic superexchange interactions destabilizes the Wigner crystal ground state, and apparently drives the system towards phase separation. As the Mn^{3+} concentration decreases further the concentration of the C-type phase increases at the expense of the Wigner crystal phase.

The phase separation which occurs from $x=0.20$ up to at least $x=0.25$ involves competing phases, both of which are antiferromagnetic, charge ordered, insulators. This distinguishes it not only from the phase separation seen from $0.12\leqslant x<0.18$, but also from the compositionally induced phase separation observed in $Nd_{0.5-x}Sr_{0.5+x}MnO_3$ (Ref. 38) and the photoinduced phase separation seen in $Pr_{1-x}Ca_xMnO_3$.[12,41] Despite the similarities the two phases exhibit distinctly different patterns of magnetic, orbital, and presumably charge order. Furthermore, the C-type phase undergoes a more abrupt transition into the charge-ordered state than the Wigner-crystal phase. In particular the distinctly different orbital ordering of these two phases provides a mechanism whereby anisotropic crystallite strains could drive the phase separation. It is also worthwhile to note that Goodenough predicted the charge, orbital, and magnetic ordering associated with the C-type phase would be most stable at $x=0.25$,[10] yet we see single-phase behavior at $x=0.18$. Others have also observed the charge ordering to be most pronounced at $x=0.18$.[27,29] Even Wollan and Koehler saw single-phase C-type magnetic ordering at $x=0.20$.[20]

The phase diagrams of $La_xCa_{1-x}MnO_3$, $Pr_xCa_{1-x}MnO_3$, and $Bi_xCa_{1-x}MnO_3$ are similar in many aspects. As previ-

ously noted by Raveau *et al.* it appears that the doping level, rather than the size of the trivalent ion, dictates the behavior of the electron-doped manganites (at least when the divalent ion is calcium).[36] Our finding that the Mn-O-Mn bond angles remain relatively constant as x increases provides a structural rationale to this observation.

V. CONCLUSIONS

Electrical, magnetic, and structural studies were performed on the electron-doped manganate system, $Ca_{1-x}Bi_xMnO_3$ ($0.03 \leqslant x \leqslant 0.25$). The crystal and magnetic structures of these samples were determined by Rietveld analysis on the x-ray and neutron powder-diffraction data. With increasing electron doping the magnetic structure of the ground state varies from a *G*-type AFM ($x \leqslant 0.03$) to a canted *G*-type AFM ($0.03 < x \leqslant 0.09$). For higher values of x ($0.09 < x < 0.18$) there is evidence of phase separation into a conducting, canted *G*-type and an insulating, AFM *C*-type phase. The $x = 0.18$ composition shows a single-phase *C*-type AFM ordering and a monoclinic crystal structure. This phase is characterized by strong orbital ordering, where all of the long Mn-O bonds line up in the same direction. Although no sign of long-range Mn^{3+}/Mn^{4+} charge ordering was observed, it seems plausible that short-range charge ordering is present. For compositions with $x > 0.18$, phase separation is also observed. The competing phases in this compositional range are the orbitally ordered, AFM *C*-type phase described above, and a phase showing orbital and magnetic ordering analogous to the Wigner crystal ordering seen in $La_{0.33}Ca_{0.67}MnO_3$. The magnetic structure can be approximated using $4a \times b \times 2c$ unit cell (where the *a*, *b*, and *c* parameters refer to the basic *Pnma* unit cell), with the moments directed in the *ac* plane. However, it is probable that the true magnetic structure is more complicated. A phase diagram is presented which should be qualitatively similar to other electron-doped systems. The wide compositional range over which phase separation is observed is particularly remarkable.

ACKNOWLEDGMENTS

Thanks to Wei Bao for pointing out the unusual behavior of this system to one of us (P.M.W.). We gratefully acknowledge Brett Hunter at ANSTO for collection of the neutron data on the $Bi_{0.18}Ca_{0.82}MnO_3$ sample, as well as Brian Toby and Barbara Reisner for assistance with the neutron data collection at the BT1 neutron powder diffractometer, Center for Neutron Research, National Institute of Science and Technology. Work at Brookhaven was supported by the U.S. Department of Energy, Division of Materials Sciences, under Contract No. DE-AC02-98-CH10886. P.M.W., P.N.S., and J. G. were supported by the Department of Chemistry at Ohio State University. W.P.L. and A.J.E. were supported in part by ONR.

[1] R. von Helmolt, B. Hozapfel, L. Schultz, and K. Samwer, Phys. Rev. Lett. **71**, 2331 (1993).
[2] C. N. R. Rao, A. K. Cheetham, and R. Mahesh, Chem. Mater. **8**, 2421 (1996).
[3] A. Urishibara, Y. Moritomo, T. Arima, A. Asamitsu, G. Kido, and Y. Tokura, Phys. Rev. B **51**, 14 103 (1995).
[4] G. H. Jonker and J. H. Van Santen, Physica (Amsterdam) **16**, 337 (1950).
[5] J. B. Goodenough and J. M. Longo, in *Magnetic and Other Properties of Oxides and Related Compounds*, Landolt-Börnstein, New Series, Group III, Vol. 4, Pt. a (Springer, New York, 1970).
[6] C. Zener, Phys. Rev. **81**, 440 (1951).
[7] A. J. Millis, P. B. Littlewood, and B. I. Shraiman, Phys. Rev. Lett. **74**, 5144 (1995).
[8] C. H. Chen, S-W. Cheong, and A. S. Cooper, Phys. Rev. Lett. **71**, 2461 (1993).
[9] C. H. Chen and S-W. Cheong, Phys. Rev. Lett. **76**, 4042 (1996).
[10] J. B. Goodenough, Phys. Rev. **100**, 564 (1955).
[11] P. G. deGennes, Phys. Rev. **118**, 141 (1960).
[12] D. E. Cox, P. G. Radaelli, M. Marezio, and S-W. Cheong, Phys. Rev. B **57**, 3305 (1998).
[13] M. Yu. Kagan, D. I. Khomskii, and M. V. Mostovoy, Eur. Phys. J. B. **12**, 217 (1999).
[14] A. Moreo, S. Yunoki, and E. Dagotto, Science **283**, 2034 (1999).
[15] J. M. Tranquada, B. J. Sternlieb, J. D. Axe, Y. Nakamura, and S. Uchida, Nature (London) **375**, 561 (1995).
[16] J. M. Tranquada, P. Wochner, and D. J. Buttrey, Phys. Rev. Lett. **79**, 2133 (1997).
[17] J. M. De Teresa, M. R. Ibarra, P. A. Algarabel, C. Ritter, C. Marquira, J. Blasco, J. Garcia, A. del Moral, and Z. Arnold, Nature (London) **386**, 256 (1997).
[18] M. Fath, S. Freisem, A. A. Menovsky, Y. Tomioka, J. Aarts, and J. A. Mydosh, Science **285**, 1540 (1999).
[19] C. Martin, A. Maignan, F. Damay, M. Hervieu, and B. Raveau, J. Solid State Chem. **134**, 198 (1997).
[20] E. O. Wollan and W. C. Koehler, Phys. Rev. **100**, 545 (1955).
[21] Z. Jirak, S. Krupicka, Z. Simsa, M. Dlouha, and S. Vratislav, J. Magn. Magn. Mater. **53**, 153 (1985).
[22] A. Maignan, C. Martin, F. Damay, and B. Raveau, Chem. Mater. **10**, 950 (1998).
[23] A. Maignan, C. Martin, F. Damay, B. Raveau, and J. Hejtmanek, Phys. Rev. B **58**, 2758 (1998).
[24] S. Mori, C. H. Chen, and S-W. Cheong, Nature (London) **392**, 473 (1998).
[25] P. G. Radaelli, D. E. Cox, L. Capogna, S-W. Cheong, and M. Marezio, Phys. Rev. B **59**, 14 440 (1999).
[26] Yimei Zhu (private communication).
[27] H. Chiba, M. Kikuchi, K. Kusaba, Y. Moraoka, and Y. Syono, Solid State Commun. **99**, 499 (1996).
[28] Y. Murakami, D. Shindo, H. Chiba, M. Kikuchi, and Y. Syono, Phys. Rev. B **55**, 15 043 (1997).
[29] W. Bao, J. D. Axe, C. H. Chen, and S-W. Cheong, Phys. Rev. Lett. **78**, 543 (1997).
[30] H. L. Liu, S. L. Cooper, and S-W. Cheong, Phys. Rev. Lett. **81**, 4684 (1998).
[31] Y. Su, C-H. Du, P. D. Hatton, S. P. Collins, and S-W. Cheong, Phys. Rev. B **59**, 11 687 (1999).
[32] C. J. Howard, C. J. Ball, R. L. Davis, and M. M. Elcombe, Aust. J. Phys. **36**, 507 (1983).

[33] A. C. Larson and R. B. Von Dreele, GSAS Software Suite, LANSCE, Los Alamos National Laboratory, Los Alamos, NM.
[34] P. N. Santhosh, A. Arulraj, P. V. Vanitha, R. S. Singh, K. Sooryanarayana, and C. N. R. Rao, J. Phys.: Condens. Matter **11**, L27 (1999).
[35] T. Vogt, A. K. Cheetham, R. Mahendiran, A. K. Raychaudhuri, R. Mahesh, and C. N. R. Rao, Phys. Rev. B **54**, 15 303 (1996).
[36] B. Raveau, A. Maignan, C. Martin, and M. Hervieu, Chem. Mater. **10**, 2641 (1998).
[37] P. Karen and P. M. Woodward, J. Solid State Chem. **141**, 78 (1998).
[38] P. M. Woodward, D. E. Cox, T. Vogt, C. N. R. Rao, and A. K. Cheetham, Chem. Mater. **11**, 3528 (1999).
[39] P. W. Anderson and H. Hasegawa, Phys. Rev. **100**, 675 (1955).
[40] D. P. Arovas and F. Guinea, Phys. Rev. B **58**, 9150 (1998).
[41] V. Kiryukhin, D. Casa, J. P. Hill, B. Keimer, A. Vigilante, Y. Tomioka, and Y. Tokura, Nature (London) **386**, 813 (1997).
[42] W. Opechowski and R. Guccione, *Magnetism* edited by G. T. Rado and H. Suhl (Academic, New York, 1963), Vol. IIA, p. 105.
[43] K. R. Poeppelmeier, M. E. Leonowicz, J. C. Scanlon, J. M. Longo, and W. B. Yelon, J. Solid State Chem. **45**, 71 (1982).
[44] C. Martin, A. Maignan, M. Hervieu, B. Raveau, Z. Jirak, A. Kurbakov, V. Trounov, G. Andre, and F. Bouree, J. Magn. Magn. Mater. **205**, 184 (1999).